DAB converter used to the BESS control operating in conjunction with a parallel active power filter

Beatriz MASQUETTI PELZ, Sérgio Augusto OLIVEIRA DA SILVA, Leonardo Bruno GARCIA CAMPANHOL, Guilherme MASQUETTI PELZ, Leonardo POLTRONIERI SAMPAIO
Federal University of Technology – Paraná (UTFPR) – Cornélio Procópio – PR, Brazil

Abstract – **This paper deals with modeling and controlling a battery energy storage system composed of a dual active bridge (DAB) converter connected to a voltage source inverter acting as a parallel active power filter (P-APF). A DAB converter control strategy is proposed to control the batteries' current using the dual-phase shift method to avoid reactive current circulation and reduce high current ripples. Thus, the battery lifetime increases, and damages could be avoided. The P-APF control is implemented through a multi-resonant state space controller. The P-APF suppresses harmonic currents and compensates for the reactive power of the load. In addition, it handles fundamental currents associated with battery charging/discharging and converter losses. Simulation results validate the control system models and evaluate the system's performance for assisting the electrical system's reliability where intermittent renewable energy sources exist.**

Index Terms – Dual-Active Bridge, Parallel active power filter, Power quality, Battery energy storage system.

1. INTRODUCTION

Nowadays, the search for reducing pollutant emissions has directed electrical energy generation towards alternative ways. In this scenario, photovoltaic and wind generation have grown considerably in recent years [1]. However, such sources have intermittent generation power, bringing challenges to the electrical system's reliability.

With the use of a battery energy storage system (BESS), it is possible to store energy during the peak generation of intermittent sources, using it at the peak demand of consumer units and bringing greater flexibility to the electrical power system for maximum use of renewable resources. In addition, energy storage systems can perform ancillary services, assisting in frequency regulation, stability, levels of voltage and power, and system power quality [2].

To allow the BESS control and its integration to the grid through a voltage source inverter (VSI), a bidirectional DC-DC converter placed between the BESS and the VSI's DC-bus is necessary. Such converters must allow bidirectional power flow, galvanic isolation, and high voltage gain [3]. For this purpose, flyback, Cuk, push-pull, forward, and dual-active bridge (DAB) are some of the converters' topologies that can be used [4].

Due to the possibility of high-power applications with high efficiency, galvanic isolation, and high voltage gain, the DAB converter has been used in several applications, such as storage systems, battery power flow control in a nano grid, systems with photovoltaic modules, and in electric vehicle chargers [5], [6]. However, depending on the control technique, the DAB converter may present reactive current circulation and a high ripple in the output current, decreasing the battery life [7]. In this paper, to overcome this problem, a dual-phase-shift (DPS) control technique is employed, which can reduce peak current, eliminate reactive power for a wide operating range, and reduce the output current oscillation [8].

Otherwise, it is possible to complement the control of the energy storage system so that it can also contribute to the energy quality of the system by filtering the currents drained from the grid by non-linear loads. In this way, the connection of the DAB converter to the grid is performed through a current-controlled VSI, operating as a parallel active power filter (P-APF) connected to the single-phase system.

Therefore, this paper aims to develop the DAB converter model integrated with a BESS and implement the control of this system operating in conjunction with a P-APF. Thus, the system can consume or supply energy to the electrical power system and provide ancillary services. Furthermore, suppressions of harmonic currents and reactive power compensating are also performed.

2. PROPOSED SYSTEM

The proposed system can be seen in Fig. 1. It comprises a full-bridge VSI, a DAB converter, and a battery bank. The current controlled VSI operates as P-APF. It is also employed to supply/absorb the battery power from the grid. The DAB converter is modeled as a controlled current source, and the battery is modeled as a lossless resistor. From these models, a multi-loop controller using proportional-integral (PI) controllers [9] was designed to regulate battery charging and discharging through the DPS technique to drive the DAB converter switches.

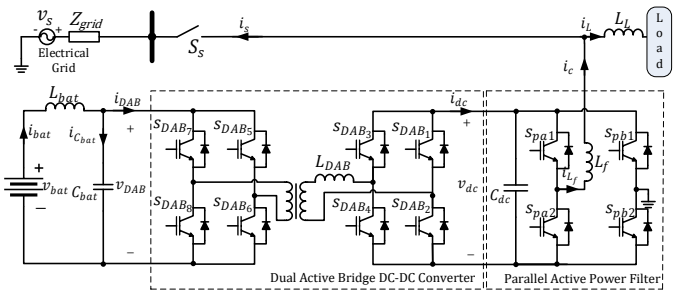

Fig. 1. Power circuit of the P-APF-DAB-BESS system.

2.1. Parallel active power filter

Regarding P-APF applied to single-phase systems, two VSI topologies are commonly employed: the half-bridge and the full-bridge configurations. The half-bridge VSI consists of two power switches and two capacitors. This configuration requires

a control loop to maintain the voltage balance between the two DC bus capacitors. In contrast, the full-bridge topology used in this work employs four power switches and a single DC bus capacitor. As a result, the required DC bus voltage is reduced by half, compared to the half-bridge configuration, and the need for DC bus voltage balancing is eliminated.

Since the objective is to suppress harmonic and reactive components of the load current, the VSI must be capable of accurately synthesizing the compensating current to be injected into the grid.

2.2. Reference generation

To ensure synchronization between the system and the single-phase power grid, the phase angle θ is obtained through a phase-locked loop (PLL) system [10]. The performance of the P-APF is assessed by its ability to synthesize the compensation current required to maintain the grid within power quality indicators, even in the presence of non-linear loads.

The current reference signal to be synthesized by the P-APF is obtained through the synchronous reference frame (SRF) method [11]. Thus, since a single-phase system has been treated, a fictitious two-phase system represented in the $\alpha\beta$ reference frame needs to be emulated. For this purpose, the direct current i_α (α-axis) is considered the own load current i_L ($i_\alpha = i_L$) and the quadrature current i_β (β-axis) is obtained by delaying the measured current i_L in 90°. After that, the fictitious two-phase system is transformed into the SRF dq-axes and the direct axis current i_d is obtained as follows:

$$i_d = i_L(\omega t)\cos\theta + i_L(\omega t - \pi/2)\sin\theta \tag{1}$$

In the synchronous frame, the continuous portion of the current i_d corresponds to the amplitude of the active component of the load current at the fundamental frequency, while the oscillating components present in i_d refer to the harmonic components of the load current. Thus, as observed in Fig. 2, a second-order low-pass filter (LPF) with a cutoff frequency of 12 Hz is used to eliminate such harmonic components, obtaining the average value $i_{d_{dc}}$.

Also, in the synchronous frame, the output of the DC link voltage controller $i_{DC_{bus}}$, represents, in a steady state, the active current component required to maintain the DC link voltage stabilized around its reference value. Thus, the reference signal for the grid current i_c^* , is calculated by subtracting the load current from the reference grid current as given by:

$$i_c^* = i_L - \left(i_{d_{dc}} + i_{DC_{bus}}\right)\cos\theta \tag{2}$$

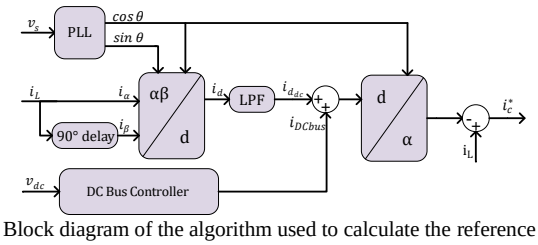

Fig. 2. Block diagram of the algorithm used to calculate the reference currents.

2.2.1. P-APF and DC Bus models

To derive the mathematical model representing the P-APF, the VSI/filter structure is analyzed using its equivalent circuit, shown in Fig. 3. In this circuit, $d(t)$ denotes the VSI control signal, V_{dc} is the DC bus voltage, L_f represents the filter inductance, R_{L_f} is the internal resistance of L_f, and $v_s(t)$ is the grid voltage.

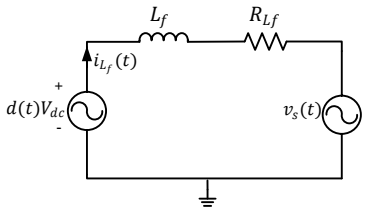

Fig. 3. Equivalent circuit of the P-APF.

From the equivalent circuit, the mathematical model is derived via the average state-space method and expressed in the following form:

$$\begin{cases} \dfrac{d\hat{\imath}_{L_f}(t)}{dt} = \underbrace{\left[\dfrac{-R_{L_f}}{L_f}\right]}_{A}\hat{\imath}_{L_f}(t) + \underbrace{\left[\dfrac{V_{dc}}{L_f}\right]}_{B}\hat{d}(t) + \underbrace{\left[\dfrac{-1}{L_f}\right]}_{B_w}\hat{v}_s(t) \\ y = \underbrace{[1]}_{C}\hat{\imath}_{L_f}(t) \end{cases} \tag{3}$$

In order to maintain the DC bus voltage at the desired value, the DC bus control provides the amplitude of the current reference that must be drained from the grid to compensate for the converter losses while maintaining the DC bus voltage regulated. Thus, to obtain the mathematical model that represents the dynamic behavior of the DC bus voltage, it is assumed that the instantaneous active power on the AC side drained by the P-APF ($p_{in_{\text{PAPF}}}$) is equal to the power in the DC bus (p_{dc}) [9], as given by:

$$\underbrace{\frac{v_{ds}i_{dc_{pc}}}{2}}_{p_{in_{\text{PAPF}}}} = \underbrace{v_{dc}i_{dc}}_{p_{dc}} \tag{4}$$

where v_{ds} is the grid voltage represented in the synchronous reference frame (SRF); $i_{dc_{pc}}$ is the active component of the current flowing through the P-APF converter; v_{dc} is the DC bus voltage and i_{dc} is the current through the DC bus capacitor.

Replacing $i_{dc} = C_{dc}\frac{dv_{dc}}{dt}$ in (4) and applying state averaging and the Laplace transform, the transfer function (TF) relating the DC bus voltage to the active current required to compensate for the P-APF losses is obtained as:

$$\frac{\hat{v}_{dc}}{\hat{\imath}_{dc_{pc}}} = \frac{v_{ds}}{C_{dc}V_{dc}s} \tag{5}$$

2.2.2. Multi-resonant state feedback controller

To allow the quantity synthesizing at different harmonic frequencies, a multi-resonant state feedback controller (SFC) is developed and implemented to control the P-APF [12]. The control methodology adopted in this work has been proposed in [13], where the SFC, based on a linear-quadratic regulator (LQR), is designed using a differential evolution (DE) metaheuristic optimization algorithm. Accordingly, the open-loop system is defined as the original P-APF model in (3), augmented by the integral of the tracking error as an additional state, along with two states per resonant term, as follows:

$$\begin{cases} \underbrace{\begin{bmatrix} \hat{x} \\ \hat{e} \\ \hat{x}_{r,1} \\ \hat{x}_{r,3} \\ \hat{x}_{r,5} \\ \hat{x}_{r,7} \\ \hat{x}_{r,9} \\ \hat{x}_{r,11} \\ \hat{x}_{r,13} \\ \hat{x}_{r,15} \end{bmatrix}}_{\hat{x}_r(t)} = \underbrace{\begin{bmatrix} \boldsymbol{A} & 0 & 0 & \cdots & 0 \\ -\boldsymbol{C} & 0 & 0 & \cdots & 0 \\ 0 & \boldsymbol{B_{r1}} & \boldsymbol{A_{r1}} & \cdots & 0 \\ \vdots & \vdots & \vdots & \ddots & \vdots \\ 0 & \boldsymbol{B_{r15}} & 0 & \cdots & \boldsymbol{A_{r15}} \end{bmatrix}}_{A_r} \underbrace{\begin{bmatrix} \hat{x} \\ \hat{e} \\ \hat{x}_{r,1} \\ \hat{x}_{r,3} \\ \hat{x}_{r,5} \\ \hat{x}_{r,7} \\ \hat{x}_{r,9} \\ \hat{x}_{r,11} \\ \hat{x}_{r,13} \\ \hat{x}_{r,15} \end{bmatrix}}_{\hat{x}_r(t)} + \underbrace{\begin{bmatrix} \boldsymbol{B} \\ 0 \\ 0 \\ 0 \\ 0 \\ 0 \\ 0 \\ 0 \\ 0 \\ 0 \end{bmatrix}}_{B_r}\hat{d}(t) + \underbrace{\begin{bmatrix} 0 \\ 1 \\ 0 \\ 0 \\ 0 \\ 0 \\ 0 \\ 0 \\ 0 \\ 0 \end{bmatrix}}_{B_{Re}}\hat{R}e(t) + \underbrace{\begin{bmatrix} \boldsymbol{B_w} \\ 0 \\ 0 \\ 0 \\ 0 \\ 0 \\ 0 \\ 0 \\ 0 \\ 0 \end{bmatrix}}_{B_{wr}}\hat{v}_s(t) \\ y(t) = \underbrace{[\boldsymbol{C} \quad 0 \quad 0 \quad \cdots \quad 0]}_{C_r}\hat{x}_r(t) \end{cases} \tag{6}$$

This system added resonant controllers of odd harmonic orders from 1 to 15. The generic matrices associated with these resonant terms are presented as follows:

$$\underbrace{\begin{bmatrix}\hat{x}_{r1}\\ \hat{x}_{r2}\end{bmatrix}}_{\hat{x}_{r,m}(t)} = \underbrace{\begin{bmatrix}0 & -(m\omega_1)^2\\ 1 & 0\end{bmatrix}}_{A_{r,m}} \underbrace{\begin{bmatrix}\hat{x}_{r1}\\ \hat{x}_{r2}\end{bmatrix}}_{\hat{x}_{r,m}(t)} + \underbrace{\begin{bmatrix}1\\ 0\end{bmatrix}}_{B_{r,m}} \hat{u}_{r,m}(t) \tag{7}$$

where $Re(t)$ is the reference signal, ω_1 is the fundamental frequency, and m is the order of the resonant terms.

Model (6) was discretized using the Tustin method and can be represented as follows:

$$\begin{cases}\hat{x}_r[k+1] = A_r^d \hat{x}_r[k] + B_r^d \hat{d}[k] + B_{Re}^d \hat{R}e[k] + B_{wr}^d \hat{v}_s[k]\\ y[k] = C_r^d \hat{x}_r[k]\end{cases} \tag{8}$$

This paper uses the LQR approach to adjust the feedback gains in the K_{LQR} state-space by the following law:

$$\hat{d}[k] = -\underbrace{[K \quad H \quad K_{res}]}_{K_{LQR}} \underbrace{\begin{bmatrix}\hat{x}[k]\\ \hat{e}[k]\\ m[k]\end{bmatrix}}_{\hat{x}_r[k]} \tag{9}$$

where K_{LQR} is the state feedback gain vector, and $\hat{x}_r[k]$ is the state vector. Moreover, K is the gain associated with the original plant states, H is the integral gain, and K_{res} is the gain vector corresponding to the resonant states.

Finally, the discretized control system is shown in Fig. 4. To obtain the K_{LQR} matrix values from LQR method, the J index performance must be minimized. Such index is defined as:

$$J = \frac{1}{2}\sum_{k=0}^{\infty} \hat{x}_r^T[k] Q_x \hat{x}_r[k] + u^T[k] R_x u[k] \tag{10}$$

where Q_x is a diagonal positive definite Hermitian or positive semidefinite matrix, in which the value of each element is related to the feedback gain of each state and R_x is a diagonal positive definite Hermitian matrix, where each element is related to the cost associated with each control input.

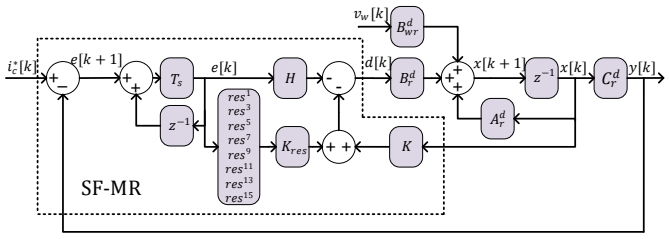

Fig. 4. Block diagram of the P-APF current control.

To obtain the values that compose the Q_x and R_x matrices, the optimization method described in [13] was used. This method is based on minimizing the following cost function:

$$C_f = w_1 THD + \frac{w_2}{t_{sim}}\sum_{k=1}^{n} kT_s|e[k]| + \frac{w_3}{t_{sim}}\sum_{k=1}^{n}(kT_s|u_{max}[k]| + kT_s|u_{min}[k]|) \tag{11}$$

where w_1, w_2 and w_3 are the weighting factors used to balance the different magnitudes of each component, as well as to regulate their importance in C_f; THD is the total harmonic distortion of the grid current; t_{sim} is the simulation time; $e[k]$ is the control loop error at iteration k; and d_{max} and d_{min} is the unit positive and negative saturation limits, respectively, of control output at iteration k.

2.3. DAB-BESS converter

The DAB converter consists of two full-bridge interconnected by a high-frequency transformer. This transformer enables a high voltage gain between the converter DC buses, resulting in a high-voltage side connected to the DC bus of the P-APF and a low-voltage side connected to the battery bank. In addition, the inductor L_{DAB} is placed between the transformer and the full-bridge on the high-voltage side. This inductor manages the voltage difference between the primary and secondary transformer sides to determine the converter's maximum power transfer capability [14] as follows:

$$P_{DAB_{max}} = \frac{n_{DAB} V_{dc} V_{DAB}}{8 f_{DAB} L_{DAB}} \tag{12}$$

where n_{DAB} is the transformer turns ratio of the DAB converter and f_{DAB} is the switching frequency of the converter.

The voltage across and current variation through L_{DAB} is controlled by the phase angle of the gate control signals of the DAB power switches. In this work, the DPS modulation technique is employed, in which two phase shift angles are used, as illustrated in Fig. 5. Specifically, Φ_{DPS_1} represents the internal phase shift angle between the switches of the first (s_{DAB_1}, s_{DAB_5}) and second (s_{DAB_3}, s_{DAB_7}) legs of the respective DAB full-bridges (see Fig. 1). Meanwhile, Φ_{DPS_2} corresponds to the external phase shift angle between the first leg of the high-voltage DAB full-bridge (s_{DAB_1}) and the first leg of the low-voltage DAB full-bridge (s_{DAB_5}).

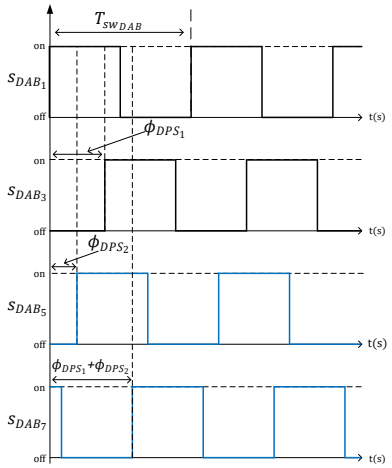

Fig. 5. Control signals of the DAB converter switches.

Due to the DAB converter voltage gain, using fewer batteries in series is possible, resulting in a lower voltage level. A battery bank with more batteries connected in parallel can be used for higher power demands.

As is well known, the battery voltage varies during charging and discharging. This study considers three main voltage levels: discharge, charge, and float. Based on these levels, the first stage of control is performed. Next, the allowable current limits for charging and discharging the battery are considered, with the first limit corresponding to 10% of the battery's maximum capacity and the second to its nominal discharge current.

2.3.1. DAB-BESS model

For achieving the required TFs for DAB-BESS control, the equivalent circuit of the converter's low-voltage side is obtained, as shown in Fig. 6. In this representation, the battery is modeled as a lossless resistor, and the DAB converter is modeled as a current source controlled by the control action defined as:

$$i_{DAB}(t) = -\frac{n_{DAB} V_{dc}}{8 f_{DAB} L_{DAB}} u_{DAB}(t) \quad (13)$$

where u_{DAB} is the control action of the DAB converter.

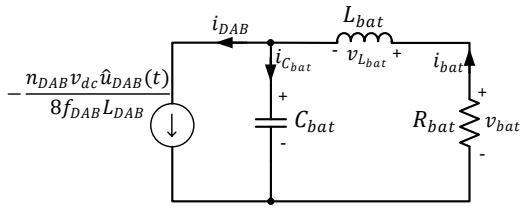

Fig. 6. Equivalent circuit of the DAB converter and BESS.

From the equivalent circuit and equation (13), the TF $G_{vi}(s)$, which relates the DAB converter voltage to the battery current, is obtained as follows:

$$G_{vi}(s) = \frac{\hat{v}_{DAB}(s)}{\hat{\imath}_{bat}(s)} = -\frac{1}{L_{bat} s + R_{bat}} \quad (14)$$

where L_{bat} is the inductance in series with the battery, R_{bat} is the resistance representing the battery and v_{DAB} is the voltage across the capacitor C_{bat} placed in the low-voltage side of the DAB converter.

By substituting the DAB converter voltage obtained from (14), the TF $G_{iu}(s)$ is derived, which relates the battery current to the converter control action, as follows:

$$G_{iu}(s) = \frac{\hat{\imath}_{bat}(s)}{\hat{u}_{DAB}(s)} = \frac{-n_{DAB} V_{dc}}{8 f_{DAB} L_{DAB}} \frac{L_{bat} s + R_{bat}}{(L_{bat} + C_{bat}) s + R_{bat}} \quad (15)$$

2.3.2. Multiloop Control

The block diagram of the multiloop controller applied to the DAB converter is shown in Fig. 7. This control strategy consists of an outer voltage loop and an inner current loop, both implemented using PI controllers. The controller's TF is given by:

$$G_{c\,v,i}(s) = \frac{K_p^{v,i} s + K_i^{v,i}}{s} \quad (16)$$

where $K_p^{v,i}$ refers to the proportional gain and $K_i^{v,i}$ refers to the integral gain of the respective voltage v and current i control loops.

The design methodology used to define the controller gains is based on 0 dB crossover frequency and phase margin specifications, as described in [9].

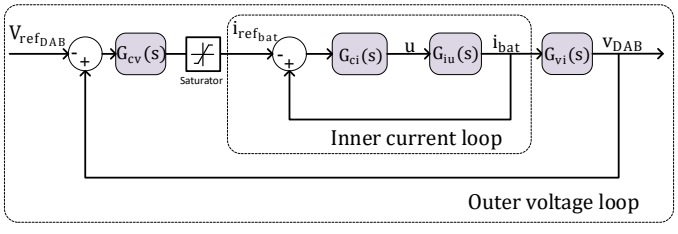

Fig. 7. Block diagram of the DAB converter control.

The outer voltage loop is responsible for defining the battery current control reference. Thus, an appropriate voltage reference is required to charge or discharge the battery. Therefore, the closed-loop TF is given by:

$$G_{MFv} = \frac{G_{cv}(s) G_{vi}(s) G_{MFi}}{1 + G_{cv}(s) G_{vi}(s) G_{MFi}} \quad (17)$$

where G_{MFi} is the TF of the inner current loop controller.

Finally, a saturator must be placed between the two control loops to ensure the battery current does not exceed the allowed amplitude.

The output of the inner current loop controller varies within the range $-1 < u_{DAB} < 1$, as defined by the control action of the DAB converter. This output adjusts the phase shift angles of the VSIs to regulate the battery current. Its closed-loop TF is given by:

$$G_{MFi} = \frac{G_{ci}(s) G_{iu}(s)}{1 + G_{ci}(s) G_{iu}(s)} \quad (18)$$

3. RESULTS

In order to evaluate the system's performance, simulations were carried out under load transient conditions for both battery charging and discharging scenarios. The P-APF was connected to a single-phase grid supplying a non-linear load, modeled as a full-bridge single-phase rectifier with an RL load. The system parameters are summarized in Table I.

The power circuit of the P-APF-DAB-BESS system, illustrated in Fig. 1, was implemented using the MATLAB/Simulink simulation environment, along with the controllers previously described. The parameters of the implemented controllers are also listed in Table I.

Table I. System and controller parameters.

Nominal RMS grid voltage	$V_{grid} = 127$ V
Nominal grid frequency	$f_{grid} = 60$ Hz
Grid impedance parameters	$L_{grid} = 50$ µH
	$R_{grid} = 0.5\ \Omega$
Filter inductance	$L_f = 1.637$ mH
Internal resistance of the filtering inductor	$R_{Lf} = 0.26\ \Omega$
Load coupling inductance	$L_L = 1.3$ mH
P-APF switching frequency	$f_{sw} = 20$ kHz
Sampling time	$T_s = (1/60\text{ k})$ s
DC link voltage	$V_{dc} = 230$ V
DC link capacitance	$C_{dc} = 2.115$ mF
DAB converter inductance	$L_{DAB} = 114$ µH
Transformer turns ratio	$n_{DAB} = 5.1$
DAB-BESS capacitance	$C_{bat} = 5.405$ mF
DAB switching frequency	$f_{DAB} = 20$ kHz
Series inductance with the batteries	$L_{bat} = 200$ µH
Rated capacity of the battery bank	6.72 kWh
Battery bank voltage	$V_{bat} = 48$ V
Battery bank resistance	$R_{bat} = 1.5\ \Omega$
Maximum discharge current of each battery	7 A
Maximum capacity per battery	28 Ah
Voltage of each battery	12 V
Number of batteries in a series (string)	4
Number of parallel strings	5
Kind of battery	Lead-acid
Full-bridge rectifier followed by *RL* load	$R = 35\ \Omega$
	$L = 25$ mH
PI controller gains - DC link voltage	$K_i = 1.1902$
	$K_P = 0.1329$
PI controller gains - DAB outer voltage loop controller	$K_i^v = 276.10$
	$K_P^v = 0.1184$
PI controller gains - DAB inner current loop controller	$K_i^i = 60.256$
	$K_P^i = 0.1031$
Weighting factors of the optimizer	
$w_1 = 45 \quad w_2 = 5 \quad w_3 = 600$	
Gain K of the current i_{L_f}	$K = 0{,}11076$
Gain H of the integral error	$H = -147.71$
Gains K_{res} of the resonant term states	
$K_{res^1} = [10\text{ k} \quad 5.7\text{ M}]$, $K_{res^3} = [8.7\text{ k} \quad 25\text{ M}]$, $K_{res^5} = [4.6\text{ k} \quad 43\text{ M}]$ $K_{res^7} = [3.4\text{ k} \quad 100\text{ M}]$, $K_{res^9} = [2.2\text{ k} \quad 160\text{ M}]$, $K_{res^{11}} = [1.1\text{ k} \quad 224\text{ M}]$ $K_{res^{13}} = [1.1\text{ k} \quad 208\text{ M}]$, $K_{res^{15}} = [2.7\text{ k} \quad 331\text{ M}]$	

Fig. 8 presents the grid voltage v_s, the grid current i_s, and the load current i_L during the battery charging and discharging processes. It can be observed that the P-APF effectively manages the absorption of current from the batteries (before 3 s) and its injection into the grid (after 3 s) while simultaneously suppressing harmonic currents and compensating for the reactive power demanded by the non-linear load.

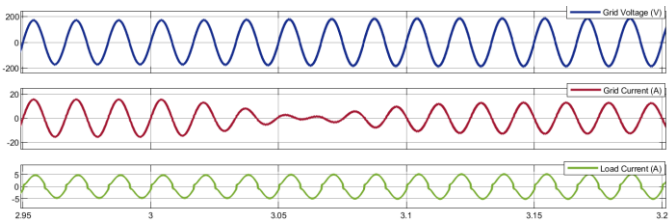

Fig. 8. Grid current, grid voltage, and load current for energy absorption/injection into the grid.

The state of charge, current, and voltage of the battery bank during the transition from battery charging to battery discharging can be observed in Fig. 9. It is noted that the battery current remained within the predefined limits, while the voltage intended to reach its reference value. Accordingly, the DAB converter control effectively manages the charging (before 3 s), discharging (after 3 s), and the transition between these stages. These scenarios validate the developed models and the DAB converter's strategy for regulating the battery current.

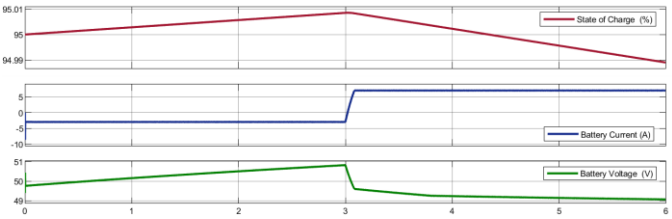

Fig. 9. Battery current, voltage, and state of charge in the load and discharge.

As observed in Fig. 8 and Fig. 9, the controls of the DAB converter and the P-APF acted in less than 0.2 s, changing the current flow direction. Firstly, up to 3s, the system was draining energy from the grid to charge the batteries. Subsequently, after 3s, the battery energy was injected back into the grid. As can be observed in Fig. 8, due to the action of the P-APF, the grid current became sinusoidal and in phase with the voltage, even in the presence of a non-linear load with total harmonic distortion (THD) of 8.82 %. As a result, the THD of the grid current was 1.03 % during battery charging and 1.68 % during battery discharging, both below the limit recommended by IEEE Standard 519 [15]. It can also be observed that when the battery was discharging, the THD of the compensated grid current increased. It is caused by the magnitude reduction of the fundamental current since the grid absorbs the difference between the energy provided by the batteries and the energy demanded by the load.

3.1. Battery Charging Operation

This Subsection presents the system behavior during the battery charging and load transients. The respective results can be observed in Fig. 10, 11, and 12. The reference voltage for charging the battery bank was set at 58 V.

Fig. 10 shows the grid voltage v_s, the grid current i_s and the load current i_L during the battery charging and the load transient at 1.5 s (50 % - 100 %). It is observed that the P-APF control compensates the grid current effectively, even in the presence of the load current disturbance.

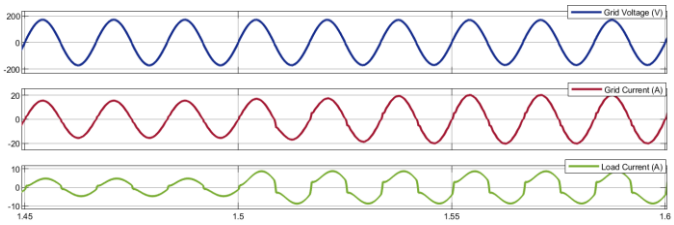

Fig. 10. Grid current and voltage, and load current for energy absorption into the grid with a load transient.

The control action of the DAB converter (u_{DAB}) is shown in Fig. 11. It has a positive value during the battery charging as defined in (13) and indicates that energy is drained from the grid. Accordingly, u_{DAB} remains constant and varies only during the load transient that occurs at 1.5 s, when the P-APF converter needs to adjust its reference to maintain a sinusoidal grid current. This event momentarily changes the power flow through the high-voltage DC bus.

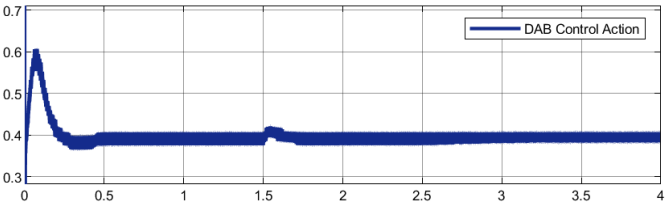

Fig. 11. DAB control action during battery charging with a load transient.

Fig. 12 presents the state of charge, current, and voltage of the battery bank. It can be observed that, despite the change in control action due to the disturbance on the high-voltage bus, this disturbance remained imperceptible on the DAB converter low-voltage side. In other words, the DAB converter control acted effectively to ensure that the load transient did not affect the battery charging behavior. It is also noted that the battery voltage and current remained within their predefined limits.

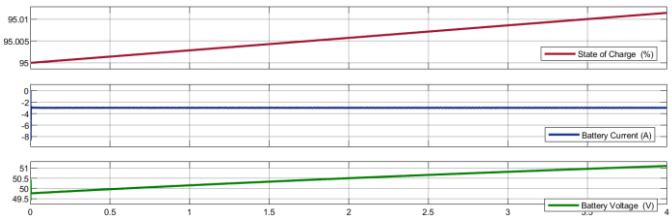

Fig. 12. Current, voltage, and state of charge during the battery charging process with a load transient.

3.2. Battery Discharging Operation

This subsection presents the system behavior during the battery discharging under load variation. The voltage reference was set to 47.9 V for battery discharging, with the same load transient at 1.5 s (50 % - 100 %). As a result, the outer voltage control loop adjusted the current reference accordingly. The DAB converter control action and other battery-related quantities yield the results shown in Fig. 13, 14, and 15.

Fig. 13 shows the grid voltage, grid current, and load current. It can be observed that, from 1.45 s to 1.5 s, the system provided all load demanded energy, and the remaining energy was injected into the grid. After the load transient (50 % - 100 %) at 1.5 s, the injected energy into the grid decreased, as can be noted by reducing the grid current amplitude once the battery bank needed to send more energy to the load. Furthermore, the system suppressed the load current's harmonic components and compensated for the reactive power.

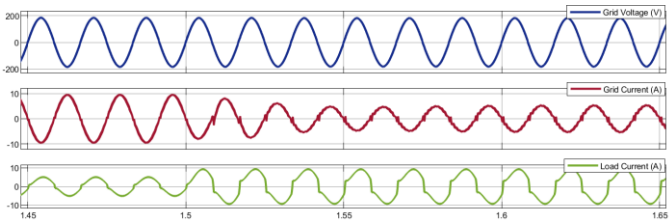

Fig. 13. Grid current and voltage, and load current for energy injection into the grid with a load transient.

The DAB converter control action (u_{DAB}) is presented in Fig. 14, where it has a negative value during battery discharging. This behavior indicates the power flow delivery to the grid, as defined in (13). It is also worth noting that, during discharging, the battery current limit is higher. As a result, the control action exhibits a greater magnitude than observed during the charging process. Moreover, a variation in the control action can be observed at 1.5 s, as the system adjusts to maintain the high-voltage bus regulated during the load transient.

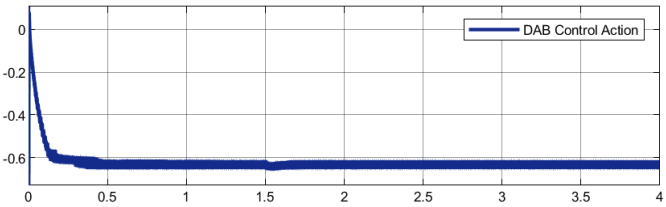

Fig. 14. DAB control action during battery discharge with a load transient.

Finally, Fig. 15 illustrates the decrease in the state of charge of the batteries, along with the battery voltage v_{bat}. The battery current i_{bat}, on the other hand, remains limited to the maximum allowable value for injection into the grid. Once again, it can be observed that, despite the disturbance in the load current, no perceptible variations occurred in the battery variables.

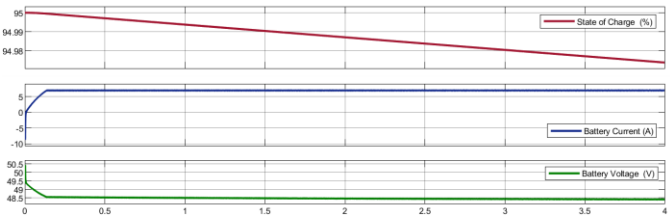

Fig. 15. Current, voltage, and state of charge during the battery discharge process with a load transient.

4. Conclusions

This paper presented the study of a BESS operating in conjunction with a P-APF. The connection between the P-APF and the BESS was carried out through the DAB converter, which was chosen due to its high efficiency in handling high power rates and ability to achieve significant voltage gains. A DAB converter model with batteries was developed to integrate the DPS technique with its control. Furthermore, a multi-resonant state feedback controller was projected and implemented for the P-APF's control. The system demonstrated that it can control active grid power's absorption and injection while compensating for the current's harmonic and reactive power of the non-linear load. Thus, the studied system represents a viable alternative for enhancing the electrical grid's reliability during peak generation periods from intermittent renewable sources and peak consumer demand. Additionally, the system contributes to improving power quality issues through active filtering.

5. Acknowledgment

The authors gratefully acknowledge the financial support from CNPq, process nº 304707/2021-0 and n° 308620/2021-6. This study was financed in part by the Coordenação de Aperfeiçoamento de Pessoal de Nível Superior - Brazil (CAPES) - Finance Code 001.

6. References

[1] J. Song, X. Zhou, Z. Zhou, Y. Wang, Y. Wang, and X. Wang, "Review of Low Inertia in Power Systems Caused by High Proportion of Renewable Energy Grid Integration," Aug. 01, 2023, Multidisciplinary Digital Publishing Institute (MDPI). doi: 10.3390/en16166042.

[2] IRENA, "Innovation landscape brief: Utility-scale batteries," Abu Dhabi, 2019.

[3] A. Rodriguez Alonso, J. Sebastian, D. G. Lamar, M. M. Hernando, and A. Vazquez, "An overall study of a Dual Active Bridge for bidirectional DC/DC conversion," in 2010 IEEE Energy Conversion Congress and Exposition, IEEE, Sep. 2010, pp. 1129–1135. doi: 10.1109/ECCE.2010.5617847.

[4] S. A. Gorji, H. G. Sahebi, M. Ektesabi, and A. B. Rad, "Topologies and control schemes of bidirectional DC–DC power converters: An overview," IEEE Access, vol. 7, pp. 117997–118019, 2019, doi: 10.1109/ACCESS.2019.2937239.

[5] V. V. Katru, M. Pattnaik, and I. Sarkar, "Dual Active Bridge Converter Control and Power Management of PV-Battery fed DC Microgrid for EV Battery Charging System," in 2023 IEEE 3rd International Conference on Smart Technologies for Power, Energy and Control, STPEC 2023, Institute of Electrical and Electronics Engineers Inc., 2023. doi: 10.1109/STPEC59253.2023.10431104.

[6] N. D. Dao, D. C. Lee, and Q. D. Phan, "High-Efficiency SiC-Based Isolated Three-Port DC/DC Converters for Hybrid Charging Stations," IEEE Trans Power Electron, vol. 35, no. 10, pp. 10455–10465, Oct. 2020, doi: 10.1109/TPEL.2020.2975124.

[7] M. Mishra and I. Sarkar, "EV Battery Charging using DAB DC-DC Converter with EPS and DPS modulations," in 2023 IEEE International Students' Conference on Electrical, Electronics and Computer Science (SCEECS), Bhopal: IEEE, Feb. 2023, pp. 1–6. doi: 10.1109/SCEECS57921.2023.10063090.

[8] H. Bai and C. Mi, "Eliminate reactive power and increase system efficiency of isolated bidirectional dual-active-bridge dc-dc converters using novel dual-phase-shift control," IEEE Trans Power Electron, vol. 23, no. 6, pp. 2905–2914, 2008, doi: 10.1109/TPEL.2008.2005103.

[9] B. A. Angélico, L. B. G. Campanhol, and S. A. Oliveira Da Silva, "Proportional-integral/proportional-integral derivative tuning procedure of a single-phase shunt active power filter using Bode diagram," IET Power Electronics, vol. 7, no. 10, pp. 2647–2659, Oct. 2014, doi: 10.1049/iet-pel.2013.0789.

[10] V. D. Bacon, S. A. O. Da Silva, L. B. G. Campanhol, and B. A. Angélico, "Stability analysis and performance evaluation of a single-phase phase-locked loop algorithm using a non-autonomous adaptive filter," IET Power Electronics, vol. 7, no. 8, pp. 2081–2092, Aug. 2014, doi: 10.1049/iet-pel.2013.0728.

[11] S. A. O. Da Silva, R. Barriviera, R. A. Modesto, M. Kaster, and A. Goedtel, "Single-phase Power Quality Conditioners with series-parallel filtering capabilities," in 2011 IEEE International Symposium on Industrial Electronics, IEEE, Jun. 2011, pp. 1124–1130. doi: 10.1109/ISIE.2011.5984202.

[12] G. M. Pelz, S. A. O. Da Silva, and L. P. Sampaio, "Distributed generation integrating a photovoltaic-based system with a single- to three-phase UPQC applied to rural or remote areas supplied by single-phase electrical power," International Journal of Electrical Power and Energy Systems, vol. 117, May 2020, doi: 10.1016/j.ijepes.2019.105673.

[13] G. M. Pelz, B. L. G. Costa, and S. A. O. Da Silva, "Tuning of state-feedback multi-resonant controllers based on LQR using differential evolution metaheuristic," International Journal of Electrical Power and Energy Systems, vol. 139, Jul. 2022, doi: 10.1016/j.ijepes.2022.107965.

[14] B. Zhao, Q. Song, and W. Liu, "Power characterization of isolated bidirectional dual-active-bridge dc-dc converter with dual-phase-shift control," IEEE Trans Power Electron, vol. 27, no. 9, pp. 4172–4176, 2012, doi: 10.1109/TPEL.2012.2189586.

[15] IEEE, 519-2014 - IEEE Recommended Practice and Requirements for Harmonic Control in Electric Power Systems. New York, 2014.